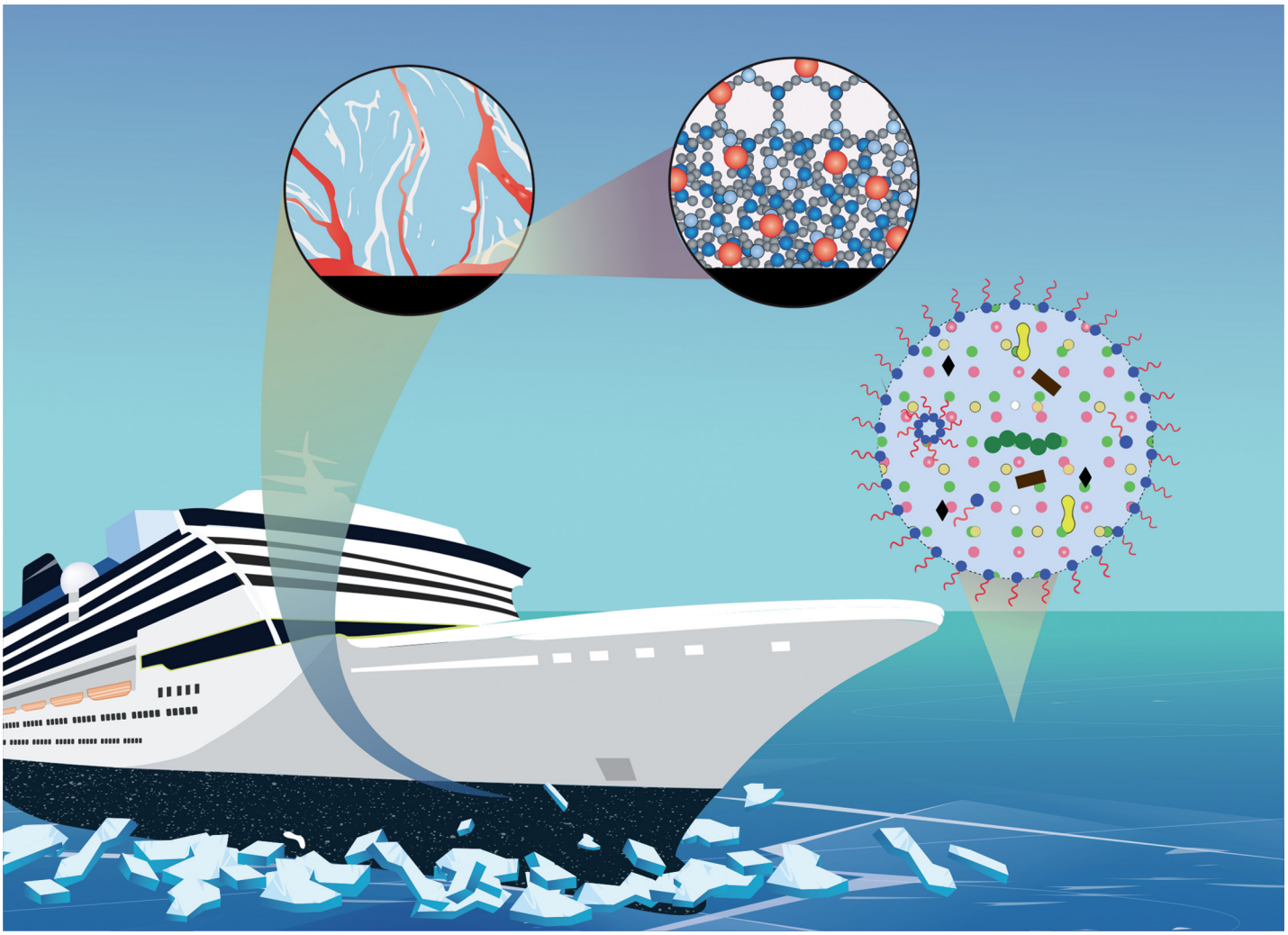

Showcasing research from Professor Sushant Anand's laboratory at the Department of Mechanical and Industrial Engineering, University of Illinois Chicago, Illinois, USA.

Adhesion of impure ice on surfaces

Impurities in ice reduce its adhesion to surfaces at moderate subcooling but result in intense adhesion at deeply subcooled temperatures. Slow freezing tends to entirely expel contaminants, forming purer ice. Conversely, rapid freezing leads to partial expulsion and an *in situ* formation of an impurity-rich liquid layer at the ice–solid interface, which weakens adhesion. Impurities also induce disorder in the adjacent ice layer, further diminishing its stickiness to surfaces.

As featured in:

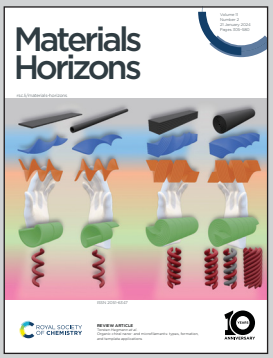

See Sushant Anand *et al.*, *Mater. Horiz.*, 2024, **11**, 419.

ROYAL SOCIETY OF CHEMISTRY

rsc.li/materials-horizons

Registered charity number: 207890

Materials Horizons

ROYAL SOCIETY OF CHEMISTRY

COMMUNICATION

Cite this: *Mater. Horiz.*, 2024, **11**, 419

Received 9th September 2023,
Accepted 21st November 2023

DOI: 10.1039/d3mh01440a

rsc.li/materials-horizons

Adhesion of impure ice on surfaces†

Rukmava Chatterjee, ‡[ab] Rajith Unnikrishnan Thanjukutty,‡[ac] Christopher Carducci, §[a] Arnab Neogi,§[a] Suman Chakraborty, [ad] Vijay Prithiv Bathey Ramesh Bapu,[ae] Suvo Banik, [a] Subramanian K. R. S. Sankaranarayanan [ad] and Sushant Anand *[a]

The undesirable buildup of ice can compromise the operational safety of ships in the Arctic to high-flying airplanes, thereby having a detrimental impact on modern life in cold climates. The obstinately strong adhesion between ice and most functional surfaces makes ice removal an energetically expensive and dangerous affair. Hence, over the past few decades, substantial efforts have been directed toward the development of passive ice-shedding surfaces. Conventionally, such research on ice adhesion has almost always been based on ice solidified from pure water. However, in all practical situations, freezing water has dissolved contaminants; ice adhesion studies of which have remained elusive thus far. Here, we cast light on the fundamental role played by various impurities (salt, surfactant, and solvent) commonly found in natural water bodies on the adhesion of ice on common structural materials. We elucidate how varying freezing temperature & contaminant concentration can significantly alter the resultant ice adhesion strength making it either super-slippery or fiercely adherent. The entrapment of impurities in ice changes with the rate of freezing and ensuing adhesion strength increases as the cooling temperature decreases. We discuss the possible role played by the *in situ* generated solute enriched liquid layer and the nanometric water-like disordered ice layer sandwiched between ice and the substrate behind these observations. Our work provides useful insights into the elementary nature of impure water-to-ice transformation and contributes to the knowledge base of various natural phenomena and rational design of a broad spectrum of anti-icing technologies for transportation, infrastructure, and energy systems.

New concepts

The development of icephobic surfaces with ice-adhesion strength of less than 10 kPa is a critical objective in applications where ice buildup poses grave problems. The measurement of ice adhesion is conventionally performed by freezing pure water. However, in practical scenarios, ice formation occurs on surfaces that contain numerous impurities. In this work, we report unprecedented findings that a mere 1 wt% of impurities can reduce ice-adhesion strength on conventional hydrophilic surfaces to <1 kPa. We show how changes in freezing temperature and contaminant concentration can significantly impact ice adhesion strength, leading to either super-slippery or fiercely adherent surfaces. We show how the freezing process affects the microstructure of brine ice that could be responsible for the formation of an *in situ* formed solute enriched liquid layer. Using MD simulations, we show how the disordered ice structure in the vicinity of a solid is affected by the presence of salt and the ice temperature. Finally, for the first time, we also provide visual evidence of impurity rejection/entrapment within a freezing droplet based on controlling the freezing rate of water to rationalize the high adhesion strength of ice on surfaces despite it being formed from impure water. Our findings offer new avenues for studying how impure ice adheres to surfaces, which has direct implications for quantifying ice repellency, understanding glacier movements, and developing freeze-protection technologies for industrial applications.

Introduction

Ice adhesion to surfaces plays a crucial role in natural processes such as glacier movement and icicle formations on rocks and cliffs, the latter adding an enchanting beauty to the winter landscape with their intricate patterns of dripping and freezing. However, it poses a multitude of problems in myriad applications as well.[1,2] For example, ice buildup on various surfaces, such as airplane wings,[3] power lines,[4] wind turbines,[5] pipelines, roads, bridges,[6] marine structures and ships,[7] can result in decreased efficiency, increased maintenance costs, hazardous conditions, and increased risk of damage and safety issues. Thus, understanding the fundamental mechanisms of ice adhesion to surfaces is crucial for developing effective de-icing technologies, improving materials with anti-icing properties,

[a] *Department of Mechanical and Industrial Engineering, University of Illinois at Chicago, USA. E-mail: sushant@uic.edu*
[b] *Carrier Corporation, 6304 Thompson Road, East Syracuse, NY, 13057, USA*
[c] *Abbott Molecular Inc., 1300 E Touhy Ave, Des Plaines, IL, 60018, USA*
[d] *Argonne National Laboratory, Argonne, IL 60439, USA*
[e] *ANSYS Inc., 10 Cavendish Ct, Lebanon, NH, 03766, USA*

† Electronic supplementary information (ESI) available. See DOI: https://doi.org/10.1039/d3mh01440a

‡ Shared first author.

§ Shared second author.

and ensuring safety in various fields, including aviation, energy production, transportation, and building design.[8,9] In this endeavor, several methods, including centrifugal and shear-removal[10–13] have been devised to measure the ice adhesion strength and then extensively used to study it on various surfaces such as common materials, non-wetting surfaces, oil-infused surfaces, gels *etc.*[11,14–19] A common element in all these studies is that the ice used in them was formed by freezing pure water. Yet, in practical scenarios, the water freezing on surfaces is rarely pure and contains a wide variety of dissolved impurities that can influence the interactions between the material's surface and freezing water, thereby affecting the resulting ice adhesion strength. For example, organic compounds, mineral dust, salts, acidic species, and biological particles are found in cloudy ice particles that are a source of icing on airplanes.[20] On marine structures, icing primarily occurs *via* sea spray which contains a wide variety of organic and inorganic impurities (Fig. 1).[21] Oceans have an average salinity level of 3.5% (or 35 000 ppm), consisting mainly of sodium and chloride ions, along with other ionic species such as magnesium, sulfate, calcium, potassium, and bicarbonate in smaller amounts.[22] Dissolved organics are also present in the ocean with an average concentration of 0.48 ppm, mainly in the form of fatty esters, free fatty acids, fatty alcohols, and surfactants (existing in the range from <0.033 to 0.52 μM).[23] Higher concentrations of organic molecules are found in the sea surface microlayer,[24] and values

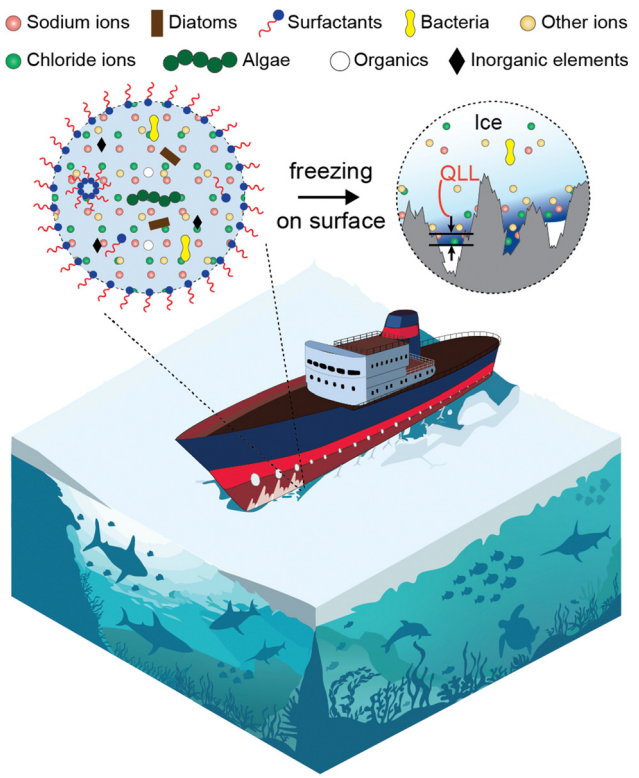

Fig. 1 Overview of the typical contaminants in water bodies which affect marine icing. Closer to ice–solid surface, a quasi-liquid layer (QLL) exists whose chemical and thermal properties could be heavily influenced by presence of impurities.

of 70–80 μmol kg^{-1} and 100 μmol kg^{-1} have been recorded in subtropical gyres and ocean margins, respectively.[22]

The presence of such dissolved substances in water can impact ice formation and adhesion by affecting the freezing temperature and the structural morphology of the resulting ice respectively. Previous studies focusing on salt's role in sea-ice formation have shown that depending upon the freezing rate, salt-rich solution (brine), may either be rejected or become trapped within the ice (homogeneously or as brine pockets).[25] Such brine pockets within the ice may have salt concentrations higher than the original salty water. Conceivably, their presence causes heterogeneity in the ice structure, leading to a non-uniform stress distribution that increases the likelihood of ice cracking, while their accumulation at the ice–solid interface may alter the ice adhesion strength. It has also been suggested that a nanometric thin layer of disordered ice, referred to as the quasi-liquid layer (QLL), forms next to a surface during the freezing of water, and plays a crucial role in ice adhesion strength.[19] Dissolved impurities can alter such ice–surface chemical interactions and the properties of this intermediate QLL. For these reasons, it is crucial to consider the effect of contaminants when studying ice adhesion. Yet surprisingly, despite its significance, this aspect hasn't received due consideration in the vast literature pertaining to ice adhesion studies over the years and several questions remain unanswered thus far.[26] For instance, the governing mechanisms which affect impure ice adhesion strength (henceforth referred as IAS) remain unclear. To what extent could the rate at which contaminated water freezes be playing a role in the resulting IAS? Does IAS vary as a function of substrate subcooling?

The current study aims at answering the abovementioned questions. We investigate the adhesion of ice formed by freezing water solutions containing varied concentrations of three different types of impurities that are representative of the common compounds found in natural water bodies: salt (sodium chloride), nonionic surfactant (Triton X-100), and solvent (ethanol) on three common industrial surfaces (copper, glass, and silicon) chilled to the Peltier surface temperature of T_{pel}. Our findings reveal that on moderately chilled surfaces, regardless of the impurity type, IAS decreases even with the presence of the tiniest amount of impurities in ice – even though the underlying surfaces are hydrophilic. Additionally with X-Ray microcomputed tomography (μCT) supported by molecular dynamics (MD) simulations we delineate how ice adhesion is affected by salt concentration and substrate subcooling which affect the geometry of channels/pockets formed inside ice and QLL thickness respectively. We also shed light on how the freezing rate alters the entrapment of such impurities, which could be potentially responsible for the high IAS observed on marine structures in frigid climates. Our results offer detailed insights into the nature of ice adhesion in the presence of impurities having far-reaching implications, which span from re-evaluating the existing construct employed for quantifying ice repellency of surfaces, understanding glacier movements, and developing freeze-protection technologies for industrial applications.

Results

Adhesion of impure ice on surfaces

We systematically investigated how various contaminant solutions adhere to industrial surfaces (*e.g.*, copper, glass, and silicon) under frigid temperature conditions (Peltier temperature, $T_{pel} = -15$ °C) by following standardized ice adhesion test protocols (see Materials and methods in ESI†). Briefly stated, a force probe connected to a force transducer exerts a shear force to a cuvette-enclosed contaminant solution frozen atop the test substrate (Fig. 2(a)). A linear increase in force is observed until the frozen column dislodges. Such behaviour is indicative of the interfacial fracture of ice on the substrate from where its IAS (τ_{adh}) is obtained (Fig. 2(b)). On all three substrates, this failure mode was observed with ice prepared by freezing pure deionized water. We tested other materials (aluminum, stainless steel, poly-tetrafluoroethylene) also, and consistently observed adhesive failure, yielding IAS values consistent with literature reports, thereby validating the reliability of our test setup and adopted protocol.[12,13] Next, we replaced pure water with 1 wt% sodium chloride aqueous solution and froze it on the copper surface under the same conditions, and repeated the experiments to obtain IAS. Here, weight percentage refers to the mass ratio of the contaminant (*e.g.*, salt) in the bulk water of the solution. For most of these tests, the force transducer measured a steady reduction after reaching the peak force, instead of an abrupt decrease (Fig. 2(b), bottom row). Despite the inherent hydrophilicity of the underlying substrate and the absence of any special surface treatments on it, the IAS measured ~1 kPa. Next, we conducted IAS experiments ($T_{pel} = -15$ °C) on all three substrates by substituting water with the aqueous solutions of sodium chloride, Triton X-100, and ethanol of varying concentrations. The concentration range for the salt and solvent was from approximately 0.003 wt% to 2 wt%, whereas for the surfactant, it was from 0.05 wt% to 4 wt%. At low impurity concentrations, adhesive failure remained predominant, but as the impurity concentration increased, sliding behaviour became common; at times accompanied by a thin liquid film trailing the dislodged frozen column. For each contaminant and concentration, six measurements were obtained. From there, we recorded the instances of adhesive failure and sliding to create a probability heat map (Fig. 2(c)) outlining the probability of failure by either mode. It is evident that the threshold concentration for each failure varies based on the contaminant and underlying surface. The sliding behaviour initiated at significantly lower concentrations of salt and solvent on glass and silicon surfaces compared to copper. On glass and silicon, at 0.00625 wt% of the solvent, the sliding behaviour was observed with its probability increasing with solvent concentration. Higher surfactant concentrations were required to trigger the sliding behaviour on silicon and copper surfaces compared to the glass. Since copper has a higher surface energy compared to glass and silicon, it forms stronger bonds with water (and ice) and adheres strongly compared to the other two test surfaces.

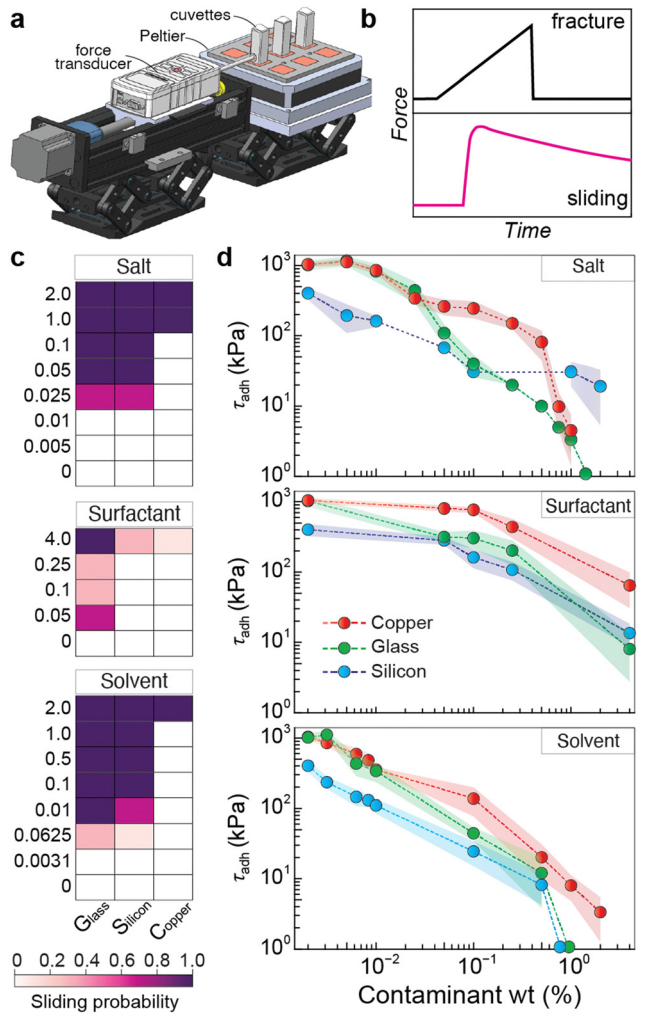

Fig. 2 Adhesion strength of impure ice on surfaces. (a) Schematic of experimental setup. (b) Qualitative illustration of the typical failure modes of ice observed in our experiments. (c) Probability heat map of the failure mechanism of contaminated ice on various surfaces. The colored scale bar in this cluster heat map represents the range of the quantitative probability of failure ranging from 0 for fracture failure (powder-pink color) to 1 for sliding failure (deep violet color). (d) Adhesion strength of impure ice on the three test substrates as a function of impurity concentration. Experiments were done following a standardized test procedure wherein, T_{pel} = −15 °C, RH ≤3%, solution freezing time = 3 h, and shear rate = 0.1 mm s^{-1}. All data points are represented as mean ± standard deviation, with the shaded band around each datapoint denoting the corresponding standard deviation.

In adhesion experiments with pure water, the sliding of the frozen ice column and the presence of interfacial liquid film trailing the cuvette is indicative of incomplete water freezing and constitute a failure that must be avoided. The presence of soluble impurities in the water can significantly increase the likelihood of the occurrence of such events due to their impact on the colligative properties of water, including the freezing point depression (ΔT_f), especially if it is similar to T_{pel}. Theoretically, $\Delta T_f = ik_f b$, where i is the van't Hoff factor, k_f is the freezing-point constant (= 1.86 K kg mol^{-1} for water), and b is the solute molarity.[27] The maximum ΔT_f of a solute is decided by its solubility limit in the solvent. For the highest salt concentration (2 wt%) used in this study, ΔT_f is of the order

of ~1.3 °C (with i = 2 for sodium chloride). Similarly, for ethanol and Triton X-100, the maximum ΔT_f is of the order of ~1 °C respectively; much smaller than the temperature (T_{pel} = −15 °C) at which bulk water was frozen to form ice for the IAS tests. So, impurity concentrations tested in our experiments were substantially below the limit necessary to inhibit ice formation in their respective solutions. Additionally, a closeup video recording of the impurity-laden solution's freezing-front movement confirmed the complete freezing of the cuvette's contents. Moreover, using a handheld plastic tweezer, we mechanically probed the frozen column in the cuvette and found no difference in its structural integrity compared to ice frozen from pure water. Such confirmatory observations suggest that the formation of the interfacial aqueous film (at a certain wt%) is a fundamental feature of the freezing process only when impurities are present.

The IAS of impure ice on the aforementioned test substrates as a function of various contaminant concentrations is showcased in Fig. 2(d). Overall, the nature of IAS reduction was similar for each impurity type across all three surfaces. IAS reduction in the presence of surfactants can be attributed to the decrease in the surface tension of water (and by extension, the surface energy of ice) that ensued by the adsorption of surfactant molecules on the hydrophilic test surfaces. However, to achieve a similar IAS reduction as observed with solvent, a nearly two-fold increase in the surfactant concentration was required. Just 1 wt% of salt or solvent was sufficient to cause a multi-fold decrease in IAS to ~0.5 kPa on glass/silicon and ~2–10 kPa on copper. IAS was most sensitive to the presence of ethanol, with even a small concentration of 0.00625 wt% reducing it by approximately 50% (1038.8 kPa to 591 kPa) on copper. Conceivably, the high surface energy of copper possibly mitigates the effect of solvent (compared to glass/silicon) to yield an overall higher IAS on it.

Temperature-dependent adhesion of saline ice

Next, to gauge whether substrate temperature can be a significant factor in IAS, we systematically investigated the adhesion of solidified brine solution on the mirror-polished copper surface over a wide window of experimental conditions using the same shear ice adhesion test procedure discussed earlier. Copper was chosen as the representative test substrate as it is a widely used industrial metal having versatile applications ranging from electronic products to building construction. Also, IAS testing was done on its smooth mirror-polished version to negate any intrinsic substrate surface roughness effects which might affect the resultant IAS quantification. The experiment consisted of varying the substrate temperature (−10 °C to −30 °C) for a wide range of salty water solution concentrations (0.005 wt% to 1 wt%) and identifying the failure mechanism (Fig. 3(a)). Upon close observation of the ice–substrate interface, three failure mechanisms were seen to occur: (I) clean shear-based 'sliding' dislodgment of the frozen solid, (II) sliding failure with the formation of an aqueous layer that reduced adhesion, and (III) mechanical interlocking of the saline ice with the base surface contributing to enhanced adhesion. At T_{pel} = −10 °C, for salt-water solution concentration between 0.005 wt% and 0.1288 wt%, clean breakage *via* shear *i.e.*, type I failure

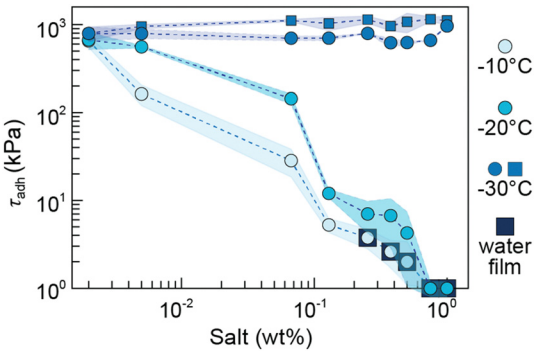

Fig. 3 Effect of temperature on IAS. Adhesion strength of saline ice as a function of substrate subcooling (RH ≤3%, water freezing time = 3 h, shear rate = 0.1 mm s^{-1}). The salt concentrations at which the interfacial aqueous film was observed post frozen column dislodgement are marked in the bottom right quadrant of the plot.

mechanism was observed. In such a scenario no residue was seen to be left behind on the substrate. From 0.2525 wt% micro drops were observed to be left behind at the saline ice-substrate (*i.e.*, copper) interface after the dislodgment of the column. At salt concentrations above 0.3762 wt%, aqueous microfilm instead of drops was observed. In this regard, it is important to note that for either of type I or II failures, the entire solid column was fully frozen during the test. So, the evolution of the aqueous film contributing to low adhesion strength stemmed from the interfacial interaction of the saline ice with the substrate. For T_{pel} = −20 °C, type I failure occurred for salt concentrations between 0.005 wt% and 0.5 wt%, while type II failure occurred from 0.75 wt% concentration. In this case, the micro drops were observed at 0.75 wt% concentration which evolved into a thin aqueous film at 1 wt% concentration. At T_{pel} = −30 °C, types I and II failures were not seen, with the breakage type of saline ice being entirely cohesive (type III). The nature of this cohesive failure can further be subdivided into two types with each occurring across all the salt-water concentrations. In some cases, only a thin whitish uniform frozen film was observed on the dislodged area post breakage (● symbol in Fig. 3(a)), while in other cases it manifested as solid ridges and chipped residue of saline ice (■ symbol in Fig. 3(a)). Quantitative measurements naturally manifested as higher IAS values for the latter case.

Preceding results make it evident that tiny amounts of impurities have a significant impact on resulting IAS and this depends upon the substrate temperature. This reduction in IAS can occur *via* two main pathways – through an *in situ* formed solute enriched liquid layer, and the changes in QLL's thickness due to the presence of solute. In the following sections we shed light on the role of both mechanisms contributing towards IAS reduction.

Mechanism of adhesion reduction of impure ice *via* brine rejection

The first plausible explanation for IAS reduction is the decrease in the solid–solid contact area between the ice and the substrate due to the *in situ* formation of a non-freezing lubricating

film as the impure water freezes. Freezing in the presence of solute has been extensively studied in the literature for various applications such as ice templating,[28,29] freezing desalination,[30] and sea ice formation.[25] For small molecules like salts/surfactants/solvents, their diffusion rate ($\sim 10^{-5}$ cm^2 s^{-1}) is much smaller than the thermal diffusivity of ice and water (10^{-2} and 10^{-3} cm^2 s^{-1} respectively) because of which steep solutes concentrations build near the ice–water interface. In regions preceding the freezing front, where the solute concentration is low, secondary nucleation may occur creating a second freezing front.[31] As a result, solutes get trapped within the two freezing layers. The solute concentration in such trapped regions can become very high, despite their low initial concentration in the virgin solution. This hinders their solidification by depressing the freezing point of the resultant solution. For salt as the solute, this phenomenon has been shown to be responsible for the formation of brine pockets trapped within the sea ice.[32] Presuming that similar behaviour occurs with other solutes also, these solute pockets can contribute to decreased IAS in two ways. Firstly, some solute pockets can stochastically form at the impure ice–substrate interface. Secondly, as solute pockets away from the interface start to freeze, their freezing cause a volume increase ($\sim$9% for brine), forcing the liquid solute out of the pockets preferentially along the grain boundaries and along the direction parallel to gravity (Fig. 4(a)).[26,33] We hypothesize that as a consequence of either mechanism, a solute enriched liquid layer (SELL) evolves at the impure ice–substrate interface contributing to the reduced IAS. The evidence of such SELL was observed in our experiments post ice column dislodgement, examples of which are shown in Fig. 4(b) for the case of 0.1 wt% and 1 wt% salty ice. Since the formation of such a layer is tied to the formation of pockets/channels and brine rejection from them, we conducted X-ray μCT experiments to study them using a custom built sample holder (Materials and methods, ESI†). We tested salty ice of varying concentrations (0.01 to 1 wt%) at three different temperatures. The ice column exhibited longitudinal optical transparency variation, with the lower portion (formed closest to the Peltier) being generally more clearer than the farther sections, (Fig. 4(c)). Consistent with the macroscopic observations, three-dimensional scans of these sections of the briny ice columns in μCT revealed a higher pocket/channel density in the mid-section of the ice column compared to the bottom section (Fig. 4(d)). Such channels/pockets form even in pure ice due to air entrapment during the freezing process (Fig. S1a–c, ESI†). Previous μCT experiments of sea ice have revealed that both brine and air pockets can form within it.[34] In our tests, the air pockets were

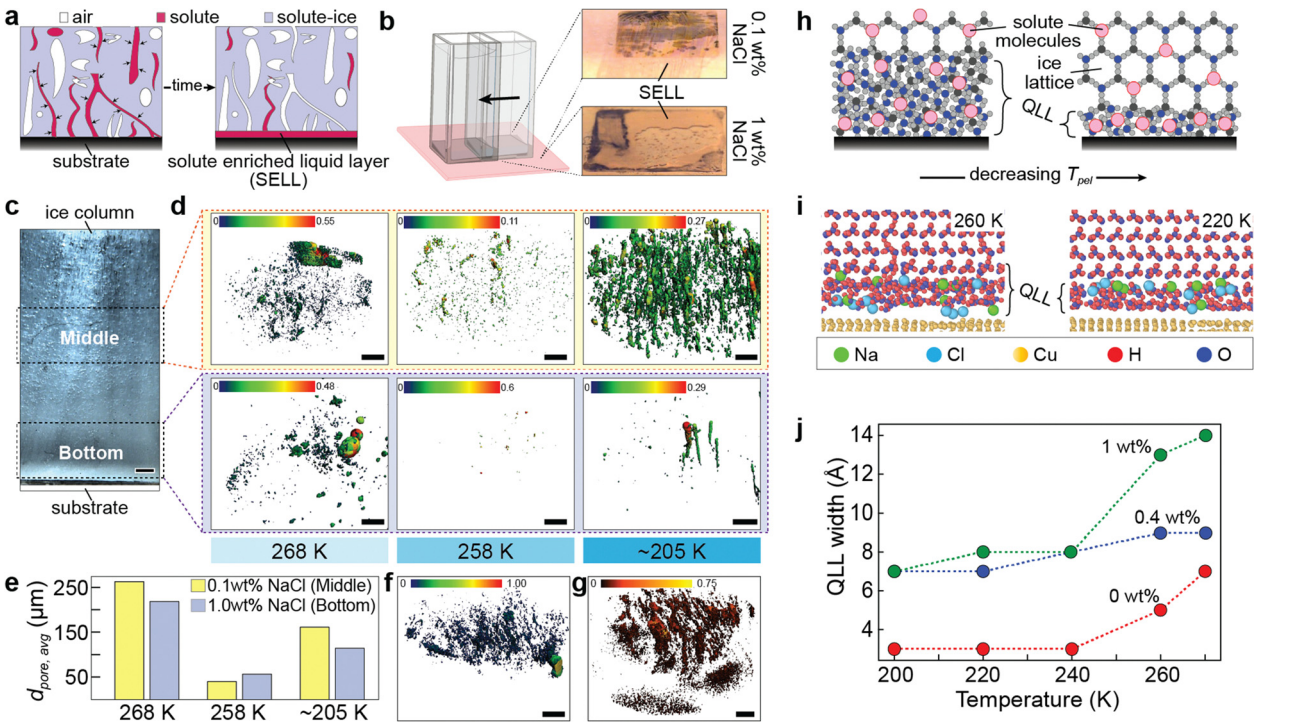

Fig. 4 Governing mechanisms behind IAS reduction in impure ice. (a) Illustration depicting drainage of solute pockets which leaves behind air channels and forms a solute enriched liquid layer (SELL) between the ice and substrate interface. (b) Example images showing evidence of SELL at −15 °C (<5%RH) for the case of 0.1 wt% and 1 wt% NaCl-ice after the ice was sheared from the surface. (c) Side-view image of an ice column formed by freezing 1 wt% NaCl solution at −15 °C (<5%RH). (d) Three-dimensional view of air channels at the middle and bottom sections of salty ice formed by freezing 0.1 wt% and 1 wt% NaCl solution respectively at three different temperatures (268 K, 258 K and 205 K). (e) Corresponding average pore diameter ($d_{pore,avg}$) in ice shown in (d). Three-dimensional views of (f) air and (g) salt channels/pores of 1 wt% CsCl in ice at −15 °C. (h) Illustration depicting the evolution of QLL with decreasing substrate cooling. (i) MD simulations results showing the QLL variation in 1 wt% NaCl doped ice for different substrate temperatures. (j) QLL width variation as a function of substrate temperature and salt (NaCl) concentration. All scale bars are 1 mm and color bars represent the pore diameter (mm).

clearly distinguishable but the brine pockets weren't (Fig. 4(d) and Fig. S1c, ESI†). This is likely because, sodium and chlorine have low attenuation coefficient (0.4 $cm^2\ g^{-1}$ and 0.9 $cm^2\ g^{-1}$ at 45 keV respectively), because of which X-rays can pass through the NaCl channels with relatively little absorption or scattering, making them almost invisible. By applying a very conservative thresholding process, we identified NaCl pockets/channels (Fig. 4(d) and Fig. S1d, ESI†), nevertheless, such identification is highly subjective and user dependent. To conclusively prove the presence of brine channels, we formed salty ice using 0.1 and 1 wt% Caesium Chloride (CsCl), leveraging Caesium's high attenuation coefficient (18.6 $cm^2\ g^{-1}$ at 45 keV)[35] and repeating μCT experiments as in the NaCl case. These representative experiments confirmed the formation of air and CsCl salt channels (Fig. 4(f) and (g)) which bolsters our original inference that similar salt channels also exist in cases of briny ice made of NaCl solution. For example, the freezing rates of briny ice formed on a highly supercooled surface are higher than sea ice that forms at lower freezing rate,[36] affecting the size/concentration of brine channels. This aspect is discussed in more detail in the penultimate section of the manuscript. It is also plausible that some of these pockets or channels initially contained a higher brine concentration which subsequently drained during the freezing process. Finally, the brine inclusions within the ice could also be smaller than the instrument's resolution (voxel size of 10 μm). Examining the details behind such possibilities is however beyond the scope of the current work and a topic for future studies. As the substrate temperature is lowered, the increased solidification could lead to a reduction in the pocket/channel size. This reduction was observed in ice formed at 268 K to 258 K (Fig. 4(d) and (e)) in both the bottom and middle sections of the ice column. However, the ice formed by freezing brine at ~205 K showed an increase in density and average pore size of open channels/pockets (Fig. 4(e)) – likely as a result of increased entrapment of air due to ultrafast freezing. Increased freezing may drive out more of the trapped solution simultaneously which potentially explains the increase in IAS as the temperature is decreased from −10 °C to −20 °C even though IAS decreased with increasing salt concentration (Fig. 3). When the substrate temperature is decreased below the limit achievable by maximum freezing point depression, the entire trapped liquid will eventually freeze. For example, with 23.225 wt% salt concentration (its eutectic limit), the maximum ΔT_f of the salt-water solution is −20.8 °C.[37] Thus IAS measurements at −30 °C are independent of salt concentration (Fig. 3) and significantly larger than that for pure water because no brine pockets or liquid layer are available to lower surface adhesion.

Mechanism of adhesion reduction of impure ice *via* QLL

While the hypothesis concerning the presence of a lubricating layer lowering the IAS is in line with the experimental observations, a secondary mechanism, which involves the alterations in the ice structure due to the presence of the solutes, may also be at play. Previous studies allude to the existence of a hydrated QLL that plays an important role in governing droplet freezing on surfaces[38] and controlling the adhesion strength of ice frozen from pure water.[19,39] As mentioned earlier, sliding failure was not explicitly perceptible for certain impurity concentrations even though the IAS was evidently decreasing (*e.g.* IAS of 0.1 wt% salt at T_{pel} = −10 °C, Fig. 3). It is possible that this decline was a result of the changes in the disordered ice layer, *i.e.* the QLL (Fig. 4(h)). The presence of impurities in water affects the thickness and chemical properties of the QLL but also creates inhomogeneities that contribute towards the slipperiness of ice.[40] Nuclear magnetic resonance spectroscopy of dilute sodium chloride aqueous solutions has shown that a similar QLL can exist at the ice surface at temperatures as low as −45 °C[41] and its thickness increases with increasing the sodium chloride concentration.[40] Since experimental limitations prohibit directly probing the presence of a QLL, we employed MD simulations to analyse the effects of temperature and salt impurities on QLL thickness (ESI†). We applied a CHILL+ algorithm[42] to ascertain the QLL thickness at the ice–substrate interface by identifying partially or fully coordinated surface molecules representing the liquid phase. The salt ions were observed to be precipitating near the ice–substrate interface, away from the bulk ice, a typical phenomenon which has been reported previously.[43] To examine the effect of salt concentration on the width of QLL, the NaCl atoms are randomly placed at the interfacial ice structure, next to the copper substrate.[44] Simulations show that the I_h (hexagonal ice) near the ice–substrate interface and the top free surface (right next to the vacuum region) amorphized within the simulation time of 1 ns at 260 K in 1 wt% salt presence. The free surface amorphization might have been triggered by the tendency of the free surface water molecules to move inwards in an attempt to form additional hydrogen bonds, which subsequently produces extra strain and disrupts the initial matrix of hydrogen bonds.[45] Fig. 4(j) depicts QLL width variation with temperature for three scenarios: no salt, 0.4% NaCl, and 1% NaCl. As the salt ions remain segregated along the ice–substrate interfacial layer, the bulk portion of ice away from the interface and free surface maintains an ordered hexagonal-ice structure. The presence of salt ions and the complex interplay between ice-ions, ice–substrate and substrate-ions induces the order-to-disorder transition in the interfacial ice structure. On similar lines, a molecular dynamics study by Vrbka *et al.*[44] explored the physics of brine rejection, in which salt ions are discharged from an ordered ice structure into the unfrozen volume of water. The increase in temperature triggers the rapid kinetic diffusion of the salt ions into the multiple layers of the ice lattice, which subsequently prompts the significant disruption of molecular ordering, leading to the formation of a thicker amorphized layer.[46] The local increase of salt ion concentration in the ice–substrate interfacial region leads to a considerable increase in the QLL width (Fig. 4(i) and (j)). The increased salt ions ease the order-to-disorder transition of hexagonal ice into bulk-like water, which triggers the growth of diffusional attributes and diminished hydrogen bonding lifetime.[46] Thus, the atomistic studies indicate that even with the presence of 0.4 wt% of salt, the QLL width surges and with increase in salt concentration to 1 wt%, the width expands remarkably at higher

temperature-observations which corroborate our macroscale ice adhesion testing results.

Why ice still adheres to ships despite low τ_{adh} of saline ice?

If small amounts of impurities can indeed drive the IAS to nearly ~1 kPa, a natural question arises as to why do marine structures in cold climates still face problems of ice adhering to their exterior forming from sea sprays (containing >3.5% salt). We hypothesize that the answer to this conundrum lies in the freezing kinetics driving the solute entrapment and rejection. The establishment of solute concentration and temperature gradients near the freezing front (described earlier) also results in the formation of instabilities at the ice–water interface.[47,48] It has been theorized that if the freezing front moves with a constant velocity (v_f), the solute distribution in the solution at a distance ξ from the interface is given by $C_{s,\xi}/C_{s,\infty} = 1 + (1/k - 1)\exp(-v_f\,\xi/D)$ for a one-dimensional system.[49] Here, k is the effective particle coefficient defined as the ratio of trapped solution concentration ($C_{s,\xi}$) to the bulk solute concentration ($C_{s,\infty}$), and D is the diffusion coefficient of solute in the liquid. It is clear from the above equation that the freezing front velocity plays a significant role in the solute distribution. However, since the surface energy of ice in the basal plane is larger than its other planes,[50] ice crystals preferably grow slightly faster along it. This results in a disparity in the solute distribution along the various facets of the growing freezing front, ultimately leading to the emergence of instabilities therein. Such instabilities can amplify over time aided by the mismatch in the surface energies across different planes of the ice crystal, leading to the formation of dendrites that can trap the contaminant particles (Fig. 5(a)). A mathematical model for the growth of such instabilities (generally referred to as the Mullins–Sekerka instabilities)[51] suggests that particle trapping occurs only when v_f exceeds a critical growth velocity (v_c)[48,49]

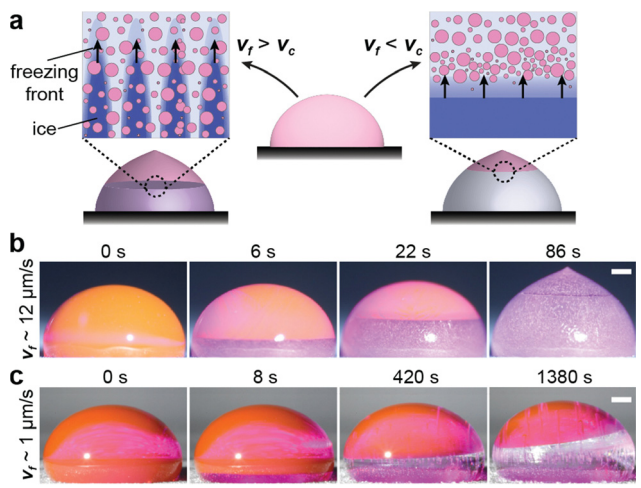

Fig. 5 Impurity entrapment and rejection (a) Schematic showing the dependence of water freezing rate on the entrapment and rejection of solutes from a liquid. Timelapse images demonstrating the axial progression of a freezing front within a dyed drop atop a hydrophobic surface cooled to T_{pel} = (b) −8 °C and (c) ~0 °C. Scale bar for (b) and (c) is 1 mm.

defined as $v_c = a_0\Delta\sigma/(3\eta R)$ where R is the radius of the particle, a_0 is the average intermolecular distance, $\Delta\sigma$ is the balance of surface forces at the ice-solution–particle interface, and η is the solution viscosity.[48] For $v_f > v_c$, particle entrapment occurs, whereas for $v_f < v_c$, rejection of all particles is possible as dendrite formation may be suppressed (Fig. 5(a)).[52] In other words, low freezing velocities are required for suppressing dendrite formation. To test this idea, we performed experiments of freezing sessile droplets of dyed water (with rhodamine B) as a function of substrate subcooling and hence different droplet freezing rates. Instead of solutes like salt/surfactant/solvent, we used dye in these experiments because the latter can make entrapment/rejection phenomenon visually perceptible. For large surface subcooling (T_{pel} = −8 °C), the freezing rates of ~12 μm s^{-1} were observed, and complete entrapment of the dye occurs (Fig. 5(b)). To get the other end of the spectrum ($v_f < v_c$), the drop freezing rate needs to be considerably decreased. This can be accomplished by maintaining surface temperatures just below 0 °C, as beyond a supercooling of 0.4 °C, instabilities grow dramatically.[53] However, such temperatures inhibit the probability of ice nucleation within drops. To resolve this issue, minute quantities of silver iodide crystals were placed on the test surface before depositing the dyed water drop on it. The substrate was then cooled to −2 °C, and as soon as the freezing front started propagating, T_{pel} was increased to just below 0 °C. In this case, almost complete rejection of the dye was observed from ~80% of the water with a corresponding freezing front velocity of ~1 μm s^{-1} (Fig. 5(c)). Although we were unable to measure IAS simultaneously in the absence/rejection of dye using this setup, we suggest that this phenomenon may play a major role in the observations of high IAS on surfaces when impure water freezes on them. Sea ice growth rates have been studied to span from 0.01 to 1 μm s^{-1}.[54] Because of such small growth rates, the planar interface remains stable as the ice shell thickens, and the resulting ice can have low salinity (<1%) compared to that of the bulk ocean. Typically measured icing rates on marine structures range from 0.1 to 10 cm h^{-1} that is 0.3 to 30 μm s^{-1}.[36] We hypothesize that the large thermal mass of the ocean surrounding isolated marine structures reduces the icing rates, and at low icing rates most of the brine is expelled from the surface during ice formation. In conjunction with our observations (Fig. 3) of the difference in entrapment and rejection as a function of freezing front velocities, we suggest that icing on marine structures is mostly devoid of brine which causes high IAS on them. Proving such a mechanism conclusively is beyond the scope of this work and needs further investigation.

Outlook

Our study shows that impurity-laden solutions can make ice slippery, which precludes the need for modifying the surface texture or material chemistry of the underlying substrate for ice-shedding applications. Our research provides a framework to re-think design possibilities for coatings that release contaminants to alter interfacial adhesion spanning applications which may require adhesion strength from low to high. However, much work is needed to resolve the many unanswered

questions that have risen from this study. For example, the mechanisms of impurity-trapped region formation (*i.e.*, solute pockets) are not fully understood. It is unclear what is the size and distribution of such pockets, how the solute enriched water drains during the freezing process and how the solute/air channels dynamically evolve for different impurities as a function of impurity concentration and ice temperature. The size of these pockets may have some dependence on solid surface properties, in particular its wettability, roughness, and thermal conductivity – aspects that need additional exploration. While we focused on three fundamental types of impurities, the range of contaminants present is way more diverse in natural environments. The investigation of how their presence (standalone or as mixtures) can affect the adhesion of complex ice structures to solid surfaces is something to consider when designing slippery surfaces for real-world icephobic applications. Future studies can also delve into uncovering the mechanisms behind the formation of the impurity-trapped region – the role played by the QLL and how its dynamic evolution varies as a function of impurity concentration and freezing temperature.

Conclusions

Over the years, studies pertaining to designing coatings that are resistant to icing have traditionally quantified icephobicity (*i.e.*, the ease with which ice can be removed from its surface) for the case of pure ice only. However, the water freezing on surfaces has an entire ecosystem of its own comprised of a multiverse of impurities. In this study, we have systematically investigated how the presence of impurities in the water can alter the freezing kinetics on a solid surface leading to changes in the resulting adhesion strength of impure ice. Our experiments with varying impurity concentrations identify the threshold concentration for adhesive failure across impurity species and base substrates. Depending upon the freezing rate and surface temperature, impurities may either get trapped within the ice or be pushed away along the freezing front. Rejection or drainage of solute enriched liquid during the freezing process could be responsible for the *in situ* formation of a non-freezing lubricating layer imparting low adhesion strength to impure ice. At the same time, MD simulations show that the presence of the contaminant also dynamically alters the interactions of the disordered liquid layer trapped between the impure ice and solid surface, that could be affecting the IAS. This study represents just the tip of the iceberg, opening new avenues for investigation of how impure ice adheres with widespread implications across multiple disciplines and industrial applications.

Author contributions

S. A. conceived, designed, and supervised the research and SKRS directed the simulation effort. R. C., R. U. T., C. C. and V. B. conducted the experiments; A. N., S. C., S. B. and S. K. R. S. conceived the simulations; A. N. performed the simulations; A. N., S. C. analysed the simulations; S. B. adapted the Chill + + algorithm for QLL analysis. A. N., S. B. and S. C. wrote the simulation section; S. A. and R. C. prepared the manuscript, and all authors provided comments.

Conflicts of interest

There are no conflicts to declare.

Acknowledgements

This work was funded by the National Science Foundation grant CBET-1805753 and CBET-1847627 (NSF CAREER). Partial support from the UIC College of Engineering is also acknowledged. Simulation studies was performed at the Centre for Nanoscale Materials, a U.S. Department of Energy (DOE) Office of Science User Facility, and supported by the U.S. DOE, Office of Basic Energy Sciences, under contract no. DE-AC02-06CH11357. The simulations are based upon work supported by the US Department of Energy, Office of Science, Office of Basic Energy Sciences Data, Artificial Intelligence, and Machine Learning at DOE Scientific User Facilities program under Award Number 34532. We thank Vincent Galavan for assistance with setup fabrication. We sincerely thank Dr Meghan Moran, Ms Rylan Martin and Dr Rick Sumner at the MicroCT/Histology Core facility of Rush University for help with the computer tomography imaging of ice and its analysis. We also thank Prof. Cort Anastasio and Dr Ted Hullar (University of California, Davis) for helpful discussions regarding μCT of ice.

References

1 K. L. Mittal and C. H. Choi, Ice Adhesion: Mechanism, *Measurement, and Mitigation*, Wiley, 2020.
2 J. Liu, C. Zhu, K. Liu, Y. Jiang, Y. Song, J. S. Francisco, X. C. Zeng and J. Wang, *Proc. Natl. Acad. Sci. U. S. A.*, 2017, **114**, 11285–11290.
3 S. G. Cober and G. A. Isaac, *J. Appl. Meteorol. Climatol.*, 2012, **51**, 265–284.
4 M. Farzaneh, *Philos. Trans. R. Soc., A*, 2000, **358**, 2971–3005.
5 F. Lamraoui, G. Fortin, R. Benoit, J. Perron and C. Masson, *Cold Reg. Sci. Technol.*, 2014, **100**, 36–49.
6 A. American Highway Users and I. H. S. G. Insight, The economic costs of disruption from a snowstorm, American Highway Users Alliance, Washington, DC, 2010.
7 T. Rashid, H. A. Khawaja and K. Edvardsen, *J. Mar. Eng. Technol.*, 2016, **15**, 79–87.
8 M. J. Kreder, J. Alvarenga, P. Kim and J. Aizenberg, *Nat. Rev. Mater.*, 2016, **1**, 15003.
9 C. Wu, H. Geng, S. Tan, J. Lv, H. Wang, Z. He and J. Wang, *Mater. Horiz.*, 2020, **7**, 2097–2104.
10 A. J. Meuler, J. D. Smith, K. K. Varanasi, J. M. Mabry, G. H. McKinley and R. E. Cohen, *ACS Appl. Mater. Interfaces*, 2010, **2**, 3100–3110.
11 A. Work and Y. Lian, *Prog. Aerosp. Sci.*, 2018, **98**, 1–26.
12 R. Chatterjee, U. Chaudhari and S. Anand, *Adv. Funct. Mater.*, 2023, **33**, 2206301.

13 R. Chatterjee, H. Bararnia and S. Anand, *Adv. Mater.*, 2022, **34**, 2109930.
14 S. A. Kulinich and M. Farzaneh, *Appl. Surf. Sci.*, 2009, **255**, 8153–8157.
15 P. Kim, T. S. Wong, J. Alvarenga, M. J. Kreder, W. E. Adorno-Martinez and J. Aizenberg, *ACS Nano*, 2012, **6**, 6569–6577.
16 H. Sojoudi, M. Wang, N. D. Boscher, G. H. McKinley and K. K. Gleason, *Soft Matter*, 2016, **12**, 1938–1963.
17 K. Golovin and A. Tuteja, *Sci. Adv.*, 2017, **3**, e1701617.
18 A. Dhyani, J. Wang, A. K. Halvey, B. Macdonald, G. Mehta and A. Tuteja, *Science*, 2021, **373**, eaba5010.
19 L. B. Boinovich, K. A. Emelyanenko and A. M. Emelyanenko, *J. Colloid Interface Sci.*, 2022, **606**, 556–566.
20 M. J. Wolf, Y. Zhang, M. A. Zawadowicz, M. Goodell, K. Froyd, E. Freney, K. Sellegri, M. Rösch, T. Cui, M. Winter, L. Lacher, D. Axisa, P. J. DeMott, E. J. T. Levin, E. Gute, J. Abbatt, A. Koss, J. H. Kroll, J. D. Surratt and D. J. Cziczo, *Nat. Commun.*, 2020, **11**, 4834.
21 T. H. Bertram, R. E. Cochran, V. H. Grassian and E. A. Stone, *Chem. Soc. Rev.*, 2018, **47**, 2374–2400.
22 X. A. Álvarez-Salgado, M. Nieto-Cid and P. E. Rossel, in *Marine Analytical Chemistry*, ed. J. Blasco and A. Tovar-Sánchez, Springer International Publishing, Cham, 2023, pp. 39–102, DOI: **10.1007/978-3-031-14486-8_2**.
23 A. A. Frossard, V. Gérard, P. Duplessis, J. D. Kinsey, X. Lu, Y. Zhu, J. Bisgrove, J. R. Maben, M. S. Long, R. Y. W. Chang, S. R. Beaupré, D. J. Kieber, W. C. Keene, B. Nozière and R. C. Cohen, *Environ. Sci. Technol.*, 2019, **53**, 9407–9417.
24 M. Cunliffe, A. Engel, S. Frka, B. Gašparović, C. Guitart, J. C. Murrell, M. Salter, C. Stolle, R. Upstill-Goddard and O. Wurl, *Prog. Oceanogr.*, 2013, **109**, 104–116.
25 R. A. Lake and E. L. Lewis, *J. Geophys. Res.*, 1970, **75**, 583–597.
26 L. Makkonen and E. Lehmus, Proc. POAC'87 Conf, 1987, 1, 45-55.
27 P. Atkins and L. Jones, *Chemical Principles: the quest for insight*, W.H. Freeman and Company, 2013.
28 S. Deville, E. Saiz and A. P. Tomsia, *Acta Mater.*, 2007, **55**, 1965–1974.
29 G. Shao, D. A. H. Hanaor, X. Shen and A. Gurlo, *Adv. Mater.*, 2020, **32**, 1907176.
30 I. Janajreh, H. Zhang, K. El Kadi and N. Ghaffour, *Water Res.*, 2023, **229**, 119389.
31 M. Grae Worster, *J. Fluid Mech.*, 1986, **167**, 481–501.
32 J. P. Terwilliger and S. F. Dizon, *Chem. Eng. Sci.*, 1970, **25**, 1331–1349.
33 M. Wakatsuchi and T. Kawamura, *J. Geophys. Res., C: Oceans Atmos.*, 1987, **92**, 7195–7197.
34 R. M. Lieb-Lappen, E. J. Golden and R. W. Obbard, *Cold Reg. Sci. Technol.*, 2017, **138**, 24–35.
35 T. Hullar and C. Anastasio, *Cryosphere*, 2016, **10**, 2057–2068.
36 S. Mintu and D. Molyneux, *Ocean Eng.*, 2022, **248**, 111501.
37 R. W. Potter, Ii, M. A. Clynne and D. L. Brown, *Econ. Geol.*, 1978, **73**, 284–285.
38 T. M. Schutzius, S. Jung, T. Maitra, P. Eberle, C. Antonini, C. Stamatopoulos and D. Poulikakos, *Langmuir*, 2015, **31**, 4807–4821.
39 D. Chen, M. D. Gelenter, M. Hong, R. E. Cohen and G. H. McKinley, *ACS Appl. Mater. Interfaces*, 2017, **9**, 4202–4214.
40 T. Mitsui and K. Aoki, *Phys. Rev. E*, 2019, **99**, 010801.
41 H. Cho, P. B. Shepson, L. A. Barrie, J. P. Cowin and R. Zaveri, *J. Phys. Chem. B*, 2002, **106**, 11226–11232.
42 A. H. Nguyen and V. Molinero, *J. Phys. Chem. B*, 2015, **119**, 9369–9376.
43 S. Blazquez, I. M. Zeron, M. M. Conde, J. L. F. Abascal and C. Vega, *Fluid Phase Equilib.*, 2020, **513**, 112548.
44 L. Vrbka and P. Jungwirth, *Phys. Rev. Lett.*, 2005, **95**, 148501.
45 D. T. Limmer and D. Chandler, *J. Chem. Phys.*, 2014, **141**, 18C505.
46 S. Deshmukh, G. Kamath, S. Ramanathan and S. K. R. S. Sankaranarayanan, *Phys. Rev. E: Stat., Nonlinear, Soft Matter Phys.*, 2013, **88**, 062119.
47 M. F. Butler, *Cryst. Growth Des.*, 2001, **1**, 213–223.
48 H. Zhang, I. Hussain, M. Brust, M. F. Butler, S. P. Rannard and A. I. Cooper, *Nat. Mater.*, 2005, **4**, 787–793.
49 G. Gay and M. A. Azouni, *Cryst. Growth Des.*, 2002, **2**, 135–140.
50 Y. Furukawa, G. Sazaki and H. Nada, *Surface and Interface Science*, Wiley-VCH Verlag GmbH & Co. KGaA, 2014, pp. 305–348, DOI: **10.1002/9783527680559.ch17**.
51 W. W. Mullins and R. F. Sekerka, *J. Appl. Phys.*, 1963, **34**, 323–329.
52 B. Rubinsky, *J. Cryst. Growth*, 1983, **62**, 513–522.
53 K. Harrison, J. Hallett, T. S. Burcham, R. E. Feeney, W. L. Kerr and Y. Yeh, *Nature*, 1988, **328**, 241–243.
54 N. S. Wolfenbarger, J. J. Buffo, K. M. Soderlund and D. D. Blankenship, *Astrobiology*, 2022, **22**, 937–961.

Electronic Supplementary Material (ESI) for Materials Horizons.

Adhesion of impure ice on surfaces

Rukmava Chatterjee[1,2†], Rajith Unnikrishnan Thanjukutty[1,3†], Christopher Carducci[1‡], Arnab Neogi[1‡], Suman Chakraborty[1,4], Vijay Prithiv Bathey Ramesh Bapu[1,5], Suvo Banik[1], Subramanian Sankaranarayanan[1,4], Sushant Anand[1*]

[1] Department of Mechanical and Industrial Engineering, University of Illinois at Chicago, USA
[2] Carrier Corporation, 6304 Thompson Road, East Syracuse, NY, 13057, USA
[3] Abbott Molecular Inc., 1300 E Touhy Ave, Des Plaines, IL, 60018, USA
[4] Center for Nanoscale Materials, Argonne National Laboratory, Argonne IL 60439, USA
[5] ANSYS Inc., 10 Cavendish Ct, Lebanon, NH, 03766, USA

† shared first author

‡ shared second author

Email: sushant@uic.edu (S.A.)

1. Materials and Methods

Synthesis of test solutions: The chemicals tested in this study (namely sodium chloride, cesium chloride, a non-ionic surfactant Triton X-100, and ethanol) were of analytical grade or higher, purchased from Sigma Aldrich, and used in their anhydrous state without further purification. De-ionized water (>99.5% purity) was purchased from Millipore-Sigma. Aqueous solutions of these chemicals were prepared by dissolving a proportionate mass of the contaminants (varying weight percentage, wt%) in a pre-measured quantity of pure water at room conditions. The mixture container was sealed, ultrasonicated for 15 min ensuring complete dissolution, and kept fully sealed until the experimentation to prevent any external contamination.

Preparation of test samples: The test substrates used for impure ice adhesion experiments were copper (Type 110, bare and mirror-polished, McMaster-Carr), glass (McMaster-Carr), and silicon (p-type, University Wafer). They were cut into 6.5 cm^2 size and cleaned by successively sonicating them in acetone, ethanol, and isopropyl alcohol for 10 min each. Samples were then dried with nitrogen gas, plasma cleaned (Herrick Plasma Etcher) to render them superhydrophilic and tested immediately.

Protocol for impure ice adhesion measurement: The adhesion strength (τ_{adh}) of various frozen contaminants was quantified by following the "peak force" method[1] adopting the protocol outlined in our earlier works.[2, 3] Experimental validation with literature data was done by virtue of rigorous benchmarking tests on commonly tested industrial materials to confirm the reliability of our test rig and adopted experimental method. All experiments were conducted inside an environmental chamber capable of precisely controlling its ambient air temperature and relative humidity while maintaining a dust-free environment. Continuous purging of the chamber with Nitrogen gas (99% pure) established ultralow humidity (RH ≤ 3%) ambient temperature (24°C) conditions which precluded any atmospheric condensation or frosting on the test surfaces (glass, silicon, copper). These test substrates (≈1 mm thick) were thermally bonded to a sample holder (with nine slots) which was directly bolted to a Peltier surface. Contaminant solutions (sodium chloride, Triton X-100, ethanol) of varying concentrations were enclosed in 1 cm^2 square plastic cuvettes (made hydrophobic prior test) and frozen for 3 h on the test substrates using the Peltier cooler. The Peltier cold plate was controlled using a PID temperature controller to establish the desired cooling temperature. Temperature of the Peltier surface (T_{pel}) and test substrates was continuously monitored using a thermocouple (Type T, OMEGA) affixed to a reference sample of the same material. The lack of any measurable temperature difference between the ice-enclosed cuvettes and cold plate justified the accuracy of the conducted tests. Independent temperature measurements also verified the absence of any spatial temperature variation across the Peltier surface, thereby ensuring experimental uniformity. In each case, it was ensured that the solutions had completely frozen before the test. Next, the cuvette-enclosed frozen columns were pushed off very close to the test substrate (<1 mm clearance between force probe from Peltier surface) with a critical shear rate of 0.1 mm/s using a force gauge (MARK-10, accuracy=±0.1%, resolution=0.01 N) mounted on a motorized translational stage (Velmex BiSlide). This methodology ensured that the impacting force didn't introduce any bending torque in the adhesion measurements. The maximum force needed for dislodging the frozen columns was recorded for each case and the corresponding τ_{adh} was calculated by dividing this measured force by the contaminant-substrate contact area. Close-up video recording (Nikon D810 camera fitted with a TAMRON macro lens) was conducted for the entire dislodgement process & after the test the interfacial contact area was immediately scrutinized to investigate the nature of the fracture: cohesive (fracture within the bulk ice phase) or adhesive (contaminant–substrate fracture). Adopting standardized experimental controls[4] adhesion experiments were repeated at least three times per sample location for each contaminant concentration to guarantee experimental accuracy and precise repeatability of reported results. A fresh specimen (substrate & solution) was used for each test to account for batch-to-batch experimental variance.

Fabrication of ice holder for micro-computer tomography (μCT) of ice: Briny ice structure was visualized using μCT by adapting protocols outlined in previous works.[5, 6] The environment inside the μCT can reach up to 40°C. Considering that an average μCT scan can last 20 minutes, imaging briny ice is a serious challenge, necessitating adequate insulation

and an internal heat sink to maintain the ice core below 0°C. Thicker insulation with a very small thermal diffusivity delays heat flow from the environment into the ice core but may attenuate and scatter the probing X-ray beam. Hence, a balance must be struck between heat transfer performance and x-ray attenuation/scattering. To enable such imaging, we fabricated a special ice-core holder assembly made with Teflon housing, surrounded by polystyrene as outer insulation material (Figure S1a). Polystyrene has negative Hounsfield units, or a radiodensity less than that of water at standard atmospheric conditions, and an estimated thermal diffusivity of 0.124 mm^2/s, so it's well suited for the chosen purpose. Teflon tubing (~1 mm thickness) was chosen due to its thermal insulative properties (α =1.54×10^{-4} mm^2/s) and radiopacity of +650 HU at 30 kV. Lastly, the heat sinks placed at the ends of the ice cores are supercooled to pull away any additional heat that may have been transferred from the insulation or during handling in sample preparation. A series of 2.5 cm-tall Teflon cylindrical cuvettes were placed on pristine glass microscope slides. These slides were cleaned prior to placement of any particulates or dust using separate rinses of ethanol and DI water. To limit the introduction of heat from the lab environment, a board of extruded polystyrene (XPS) insulation had tube-sized holes bored through to surround the cuvettes during the freezing process. The Peltier was then dropped to the chosen supercooled temperature. Brine water of known wt% NaCl filled the cuvettes and frozen. At least two hours passed during the freezing process to ensure that the entirety of the brine solution was completely frozen.

Protocol for μCT of ice and image analysis: Once fully assembled, the 34 mm ID sample holder was placed in the μCT-scanner (ScanCo microCT 40), and an initial scout-view (Figure S1a) displays the lengthwise cross-section of the assembly. Using the SCANCO Medical μCT systems suite, a cylindrical volume of interest (VOI) of 10 mm and a diameter of 36.88 mm was selected giving a VOI of about 10,682 mm^3. The voxel size was 10 μm at an acceleration voltage of 45 kV, intensity of 177 μA, sample time of 200 ms, and rotation interval of 0.18°. For image analysis, we used ScanCo's software for manipulating raw images to remove noise and ring artifacts before thresholding them (Figure S1b). For this image analysis, the segmentation units were chosen in mg HA/ccm, the Gauss sigma value was 2.8, the Gauss support value was 6, the Lower threshold was -45.0, and the Upper threshold value was 3000.0. After thresholding, the image sequences were converted into a 3D pore map profile (Figure S1c). *Note that* existing literature for the thresholding values for concentrated salts solutions, or salts in general is sparse. One approach finds the linear attenuation coefficient of a mixture (μ) as the sum of the constituent elemental linear attenuation coefficients (μ_i) such that $\mu = \Sigma^N{}_i \, \mu_{i_a} N_i$, where N_i = [# atoms of element i]/cm^3 and $\mu_{i_a} = \mu_i / N_i$ with μ_i being dependent on the X-ray beam voltage.[7] However, since the number density of salt ions is variable and unknown in frozen precipitates of salt, the exact value of μ for Cesium Chloride (CsCl) and NaCl found in the salty ice cannot be exactly determined. Practically, then μ can be estimated directly from scan results. By adjusting the lower threshold of grayscale values such that brightly valued pixels are the only pixels made white in the binary image transform, the value of μ can be experimentally estimated for each respective salt. This method's efficacy relies on defining the soft boundary edges of salt channels, potentially introducing bias by either excluding diffused salt as noise or including bright noise as salt. In this work, the linear attenuation coefficients for CsCl and NaCl were chosen to be 1.22 and 1.05, respectively. With these respective thresholding values, the image sequences were converted into 3D salt channel profiles (Figure S1d and S1e).

Statistical analysis: The reported data were obtained through necessary normalization, whereby the obvious outliers (if any) were excluded after comprehensive experimentation and validation. All data are showcased as mean±standard deviation, with the associated error bars representing the corresponding standard deviations obtained from independent experimentation of each sample, repeated three times each (unless stated otherwise). Experimental data was analyzed in OriginPro software and plotted using Adobe Illustrator.

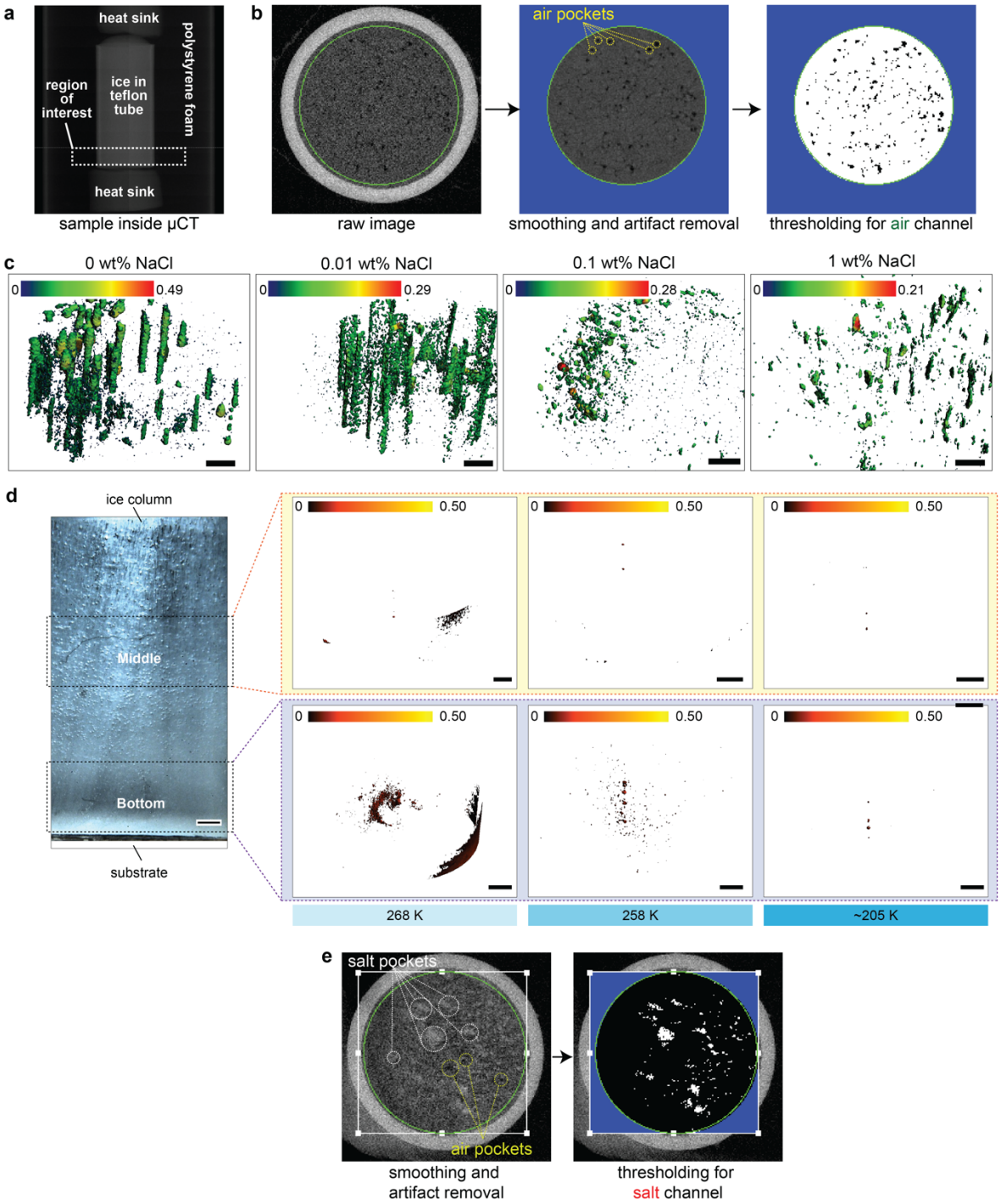

Figure S1. (a) Scout-view of the sample. **(b)** Image analysis process to threshold images to visualize air channels in ice with sodium chloride (NaCl). The dark black regions in the image show air channels. **(c)** 3D images of air channels/pores in ice at temperature of −15°C for different salt concentrations. Increasing the salt concentration decreases air pocket size and density because it leads to the formation of ice crystals with reduced space for air pockets. **(d)** Front-view image of ice formed by freezing salty water in a cuvette on a Peltier device at −15°C. Also shown are the 3D images of salt channels/pores in ice for 0.1 wt% NaCl (medium section) and 1 wt% NaCl (bottom section) at different temperatures. The air-channels for the same sections are shown in Figure 4 of the main manuscript. **(e)** Image analysis process to threshold images to visualize salt channels in ice with Cesium Chloride (CsCl). Scale bar: 1 mm. Color bar represents pore diameter (mm).

2. Molecular Dynamic (MD) simulations

Hexagonal ice (I_h) slab (with {111 terminating surface orientation) is placed on a {100} Copper (Face Centered Cubic) block acting as a wall material and the corresponding amorphization at the wall-ice interface is investigated for three different cases. The baseline simulation includes pure I_h on a copper block, the setup for which is shown in Figure S2b, the interface quasi-liquid layer (QLL) thickness is then compared with randomly infused ≈ 0.4wt % (model depicted in Figure S2a) and ≈ 1 wt% of salt (NaCl) impurities at the interface that is within 10 Å from the wall materials. The dimension of the simulation box is 46 × 26.6 × 85 Å3 which includes a vacuum region on top of the I_h slab of ≈ 17 Å.

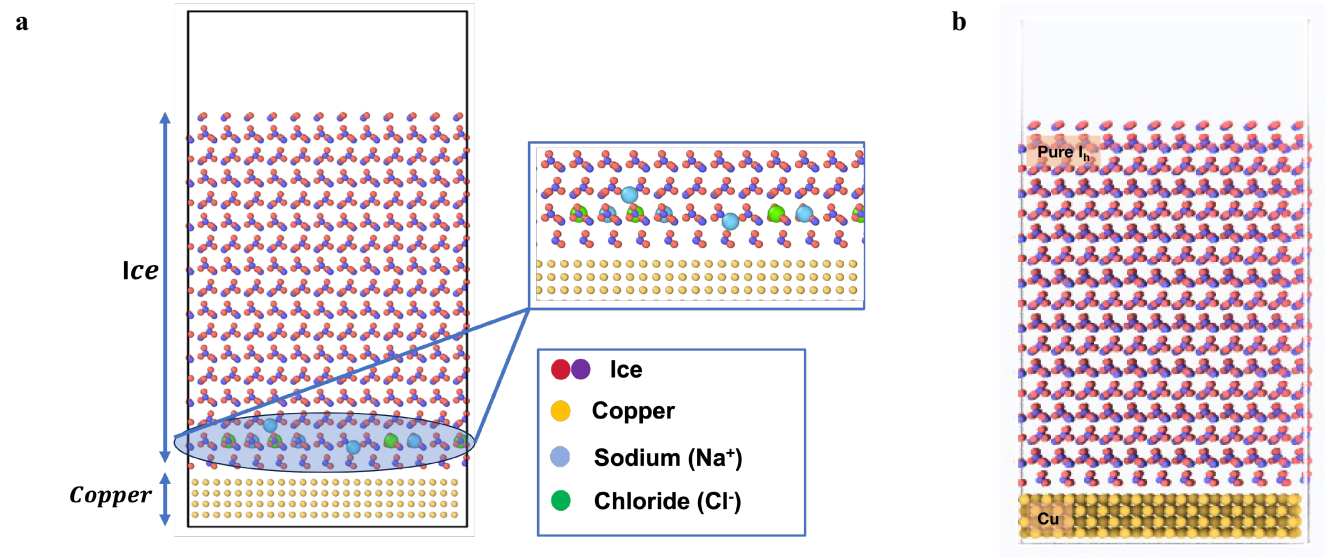

Figure S2. (a) Molecular Dynamics Setup of 0.4 wt% of NaCl doped at the interface of ice and Cu interface. **(b)** Pure ice is simulated with Cu wall for different temperatures.

The charge of oxygen and hydrogen atoms are -1.1128e and 0.5564e respectively[8] while the impurity dopants, Na^+ and Cl^- ions are assigned to have +1e and -1e and the Copper atoms are however kept neutral. The ions are randomly positioned at the Oxygen sites near the wall interface and the respective Hydrogen atoms with their related bond information are removed. The general purpose all-atom potential model TIP4P/2005 is applied to capture the water molecule interactions, the Embedded Atom Method interatomic potential is used for Cu-Cu interaction[9] and Lennard-Jones (LJ) parameters capture the cross interaction between Cu-Water[10], NaCl-Water[11] molecules. The Morse style interatomic potential is used for the cross interaction between the wall and salt ions[12]. The 12-6 LJ potential equation[13] is represented by a steep repulsive part and a smooth attractive part as a function of separation distance, $U(r) = 4\varepsilon\left[\left(\frac{\sigma}{r}\right)^{12} - \left(\frac{\sigma}{r}\right)^{6}\right]$ whereas the Morse interaction is represented by the equation $U(r) = D_0\left[e^{-2\alpha(r-r_0)} - 2e^{-\alpha(r-r_0)}\right]$, where D_0, α, and r are the potential well depth, the width of the potential well and the separation distance (<cut-off radius, r_c) respectively. The cut-off radius for the TIP4P/2005 is 13 Å and 3 Å for both LJ and Morse potential forms. The water bonds and angles are constrained by the SHAKE algorithm and periodic boundary conditions are applied in the x-y direction keeping the z boundary is fixed. The steered MD simulations are performed with the open-source platform, LAMMPS (Large-scale Atomic/Molecular Massively Parallel Simulator)[14] with each timestep of 1 fs. The system temperature is varied from 200 K to 270 K and is controlled by the combination of NVE and Langevin ensemble.

System analysis description: Chill+ algorithm: The QLL thickness at the ice-wall interface is calculated using CHILL+ algorithm based on Oxygen sites. The identification of QLL (quasi-liquid layer) involves determining partially or fully coordinated surface molecules that belong to the liquid phase. To accomplish this, we utilize the CHILL+ algorithm.[15]

The CHILL+ algorithm incorporates the correlated bond-order parameters developed by Steinhardt et al.[16] to facilitate this identification process. The local order of rank around each water molecule is determined using the aforementioned bond order parameter vectors. The principal idea is to identify staggered (S) and eclipsed (E) bonds. By utilizing this orientational order parameter, a "c" parameter is between a pair of molecules, using the equation $c(i,j) = \frac{q_i.q_j}{|q_i||q_j|}$. Where the q_i local orientational bond order parameter vector comprising of complex components around the four nearest neighbors of each molecule. A staggered bond is identified when c(i, j) ≤ −0.8, while an eclipsed bond is identified when $-0.05 \geq c(i,j) \geq -0.2$. Based on the predefined number of eclipsed and staggered bonds in hexagonal ice[15], all the crystalline particles are identified, and the remaining particles are labeled as liquid particles belonging to the QLL layer. The aforementioned CHILL+ algorithm is employed in the OVITO[17] package for the identification of the liquid particles. Subsequently, the thickness of the QLL is determined in simulations at different salt concentrations and temperatures to investigate their effects on the QLL thickness. Only the amorphization at the ice-wall interface is accounted for in the QLL width calculations.

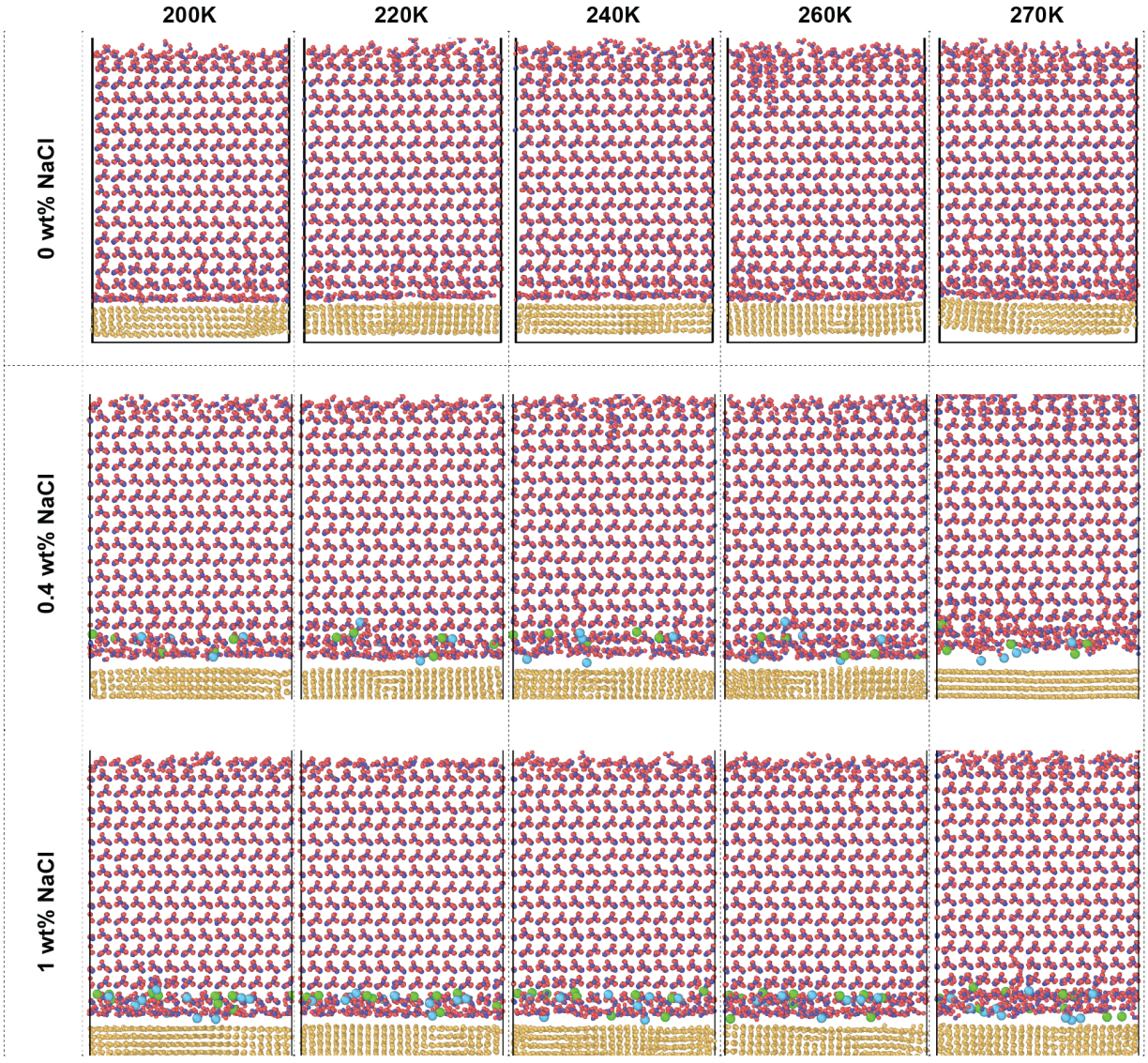

Figure S3. Results of simulations of different temperatures and salt concentrations.

REFERENCES

1. A. J. Meuler, J. D. Smith, K. K. Varanasi, J. M. Mabry, G. H. McKinley and R. E. Cohen, *ACS Appl. Mater. Interfaces*, 2010, **2**, 3100-3110.
2. R. Chatterjee, U. Chaudhari and S. Anand, *Adv. Funct. Mater.*, 2022, DOI: 10.1002/adfm.202206301, 2206301.
3. R. Chatterjee, H. Bararnia and S. Anand, *Adv. Mater.*, 2022, **34**, 2109930.
4. P. Irajizad, S. Nazifi and H. Ghasemi, *Adv. Colloid Interface Sci.*, 2019, **269**, 203-218.
5. T. Hullar and C. Anastasio, *Cryosphere*, 2016, **10**, 2057-2068.
6. R. M. Lieb-Lappen, E. J. Golden and R. W. Obbard, *Cold Reg. Sci. Technol.*, 2017, **138**, 24-35.
7. D. F. Jackson and D. J. Hawkes, *Phys. Rep.*, 1981, **70**, 169-233.
8. J. L. F. Abascal and C. Vega, *J. Chem. Phys.*, 2005, **123**.
9. S. M. Foiles, M. I. Baskes and M. S. Daw, *Phys. Rev. B*, 1986, **33**, 7983-7991.
10. T. Lin, X. Quan, P. Cheng, J. Li and G. Chen, *Int. J. Heat Mass Transfer*, 2020, **163**.
11. A. L. Benavides, M. A. Portillo, V. C. Chamorro, J. R. Espinosa, J. L. F. Abascal and C. Vega, *J. Chem. Phys.*, 2017, **147**.
12. C. G. Guymon, R. L. Rowley, J. N. Harb and D. R. Wheeler, *Condens. Matter Phys.*, 2005, **8**, 335-356.
13. J. E. Jones, *Proc. Roy. Soc. London A*, 1924, **106**, 441-462.
14. A. P. Thompson, H. M. Aktulga, R. Berger, D. S. Bolintineanu, W. M. Brown, P. S. Crozier, P. J. in 't Veld, A. Kohlmeyer, S. G. Moore, T. D. Nguyen, R. Shan, M. J. Stevens, J. Tranchida, C. Trott and S. J. Plimpton, *Comput. Phys. Commun.*, 2022, **271**.
15. A. H. Nguyen, M. A. Koc, T. D. Shepherd and V. Molinero, *J. Phys. Chem. C*, 2015, **119**, 4104-4117.
16. P. J. Steinhardt, D. R. Nelson and M. Ronchetti, *Phys. Rev. B*, 1983, **28**, 784-805.
17. A. Stukowski, *Modell Simul Mater Sci Eng*, 2010, **18**.